



Article

Local Structure and Redox Properties of Amorphous CeO₂-TiO₂ Prepared Using the H₂O₂-Modified Sol-Gel Method

Myungju Kim ¹, Gwanhee Park ² and Heesoo Lee ^{1,*}

¹ Department of Materials Science and Engineering, Pusan National University, Busan 46241, Korea; myungjukim@pusan.ac.kr

² Graduate School of Convergence Science, Pusan National University, Busan 46241, Korea; gwanheepark@pusan.ac.kr

* Correspondence: heesoo@pusan.ac.kr; Tel.: +82-51-510-2388; Fax: +82-51-512-0528

Abstract: Amorphous CeO₂-TiO₂ nanoparticles synthesized by the H₂O₂-modified sol-gel method were investigated in terms of the Ce-O-Ce and Ti-O-Ti linkage, local structure, and redox properties. The decrease in the crystallinity of CeO₂-TiO₂ by H₂O₂ addition was confirmed. The metal-oxygen linkage analysis showed the difference in size of the metal-oxygen network between crystalline CeO₂-TiO₂ and amorphous CeO₂-TiO₂ due to the O₂²⁻ formed by H₂O₂. The local structure of CeO₂-TiO₂ was analyzed with an extended X-ray absorption fine structure (EXAFS), and the oscillation changes in the k space revealed the disordering of CeO₂-TiO₂. The decrease in Ce-O bond length and the Ce-O peak broadening was attributed to O₂²⁻ interfering with the formation of the extended metal-oxygen network. The temperature-programmed reduction of the H₂ profile of amorphous CeO₂-TiO₂ exhibited the disappearance of the bulk oxygen reduction peak and a low-temperature shift of the surface oxygen reduction peak. The H₂ consumption increased compared to crystalline CeO₂-TiO₂, which indicated the improvement of redox properties by amorphization.

Keywords: CeO₂-TiO₂ nanoparticle; metal-oxygen linkage; peroxy ions; disordered oxygen; redox property



Citation: Kim, M.; Park, G.; Lee, H. Local Structure and Redox Properties of Amorphous CeO₂-TiO₂ Prepared Using the H₂O₂-Modified Sol-Gel Method. *Nanomaterials* **2021**, *11*, 2148. <https://doi.org/10.3390/nano11082148>

Academic Editor:
Yiannis Deligiannakis

Received: 2 August 2021
Accepted: 19 August 2021
Published: 23 August 2021

Publisher's Note: MDPI stays neutral with regard to jurisdictional claims in published maps and institutional affiliations.



Copyright: © 2021 by the authors. Licensee MDPI, Basel, Switzerland. This article is an open access article distributed under the terms and conditions of the Creative Commons Attribution (CC BY) license (<https://creativecommons.org/licenses/by/4.0/>).

1. Introduction

Metal oxides have been widely studied in from a number of research angles, including their uses in catalysts, in electrochemistry, and as gas sensors [1]. Cerium oxide, CeO₂, is an important rare-earth oxide with a redox pair of Ce³⁺/Ce⁴⁺, which enables the storage/release of oxygen located at the tetrahedral site under an oxidation/reduction atmosphere [2]. However, CeO₂ is mainly used with other metal oxides because of its low redox property, specific surface area, and the thermal stability of pure CeO₂. TiO₂ has been extensively investigated as a CeO₂-TiO₂ mixed oxide due to its advantages, such as a highly specific surface area, outstanding thermal and chemical stability, and non-toxicity. CeO₂-TiO₂ nanoparticles have attracted much interest for use in various areas where oxidation/reduction reactions of cerium ions are important, such as de-NO_x catalysts, photocatalysts, and water gas shift catalysts [3–5]. CeO₂-TiO₂ nanoparticles have various properties depending on their crystallinity, and many studies have reported the improvement of the catalytic performance of CeO₂ and TiO₂ through amorphization [6,7].

Amorphous oxides have great potential, and their method of synthesis has been highlighted, as amorphous oxides have excellent physicochemical properties compared to crystalline oxides [8]. CeO₂-TiO₂ nanoparticles are synthesized by the sol-gel method, hydrothermal routes, and coprecipitation [9–11]. The sol-gel method is widely used and has the advantages of obtaining uniform particles and a highly specific area [12]. The structure of the oxide synthesized through this method is modified according to the degree of hydrolysis, which is affected by additives or the amount of H₂O [13,14]. Modifying the hydrolysis and condensation reaction causes changes in structure—for

example, in the crystallinity and microstructure [15–17]. Therefore, it is important to understand the mechanism of hydrolysis and condensation reactions in terms of local structure in the sol-gel reaction and to reveal the relationship between structural properties and physicochemical properties.

In this study, the metal–oxygen linkage, local structure, and redox properties of CeO₂-TiO₂ nanoparticles were synthesized by the H₂O₂-modified sol-gel method. The effect of H₂O₂ on the linkage in the sol-gel was verified by Fourier transform infrared spectroscopy. The local structure was analyzed using an extended X-ray absorption fine structure (EXAFS). The relationship between the local structure and the redox properties was examined by H₂-temperature-programmed reduction.

2. Experimental Procedure

2.1. Sample Preparation

The samples were synthesized by the sol-gel method with a molar ratio of Ce:Ti = 3:7; cerium nitrate and titanium isopropoxide (TTIP, Ti[OCH(CH₃)₂]₄, Sigma-Aldrich, St. Louis, MO, USA, 97%) were used as precursors of CeO₂ and TiO₂, respectively. TTIP was added to ethanol while stirring. Here, we added H₂O₂ at a volume ratio of TTIP:35% H₂O₂ = 1:5 after the addition of TTIP. Distilled water was poured into the mixed solution to start the hydrolysis of TTIP. Cerium nitrate hexahydrate (Ce(NO₃)₃ · 6H₂O, Sigma-Aldrich, St. Louis, MO, USA, 99%) was added to the mixed solution, then ammonia hydroxide solution (NH₄OH 25% in H₂O, Junsei, Tokyo, Japan) was slowly added until the pH of the mixed solution reached approximately 10. The filtered precipitate was dried at 80 °C and calcined at 550 °C to obtain a CeO₂-TiO₂ powder. The prepared oxides were named CT and CT_H₂O₂ according to the H₂O₂ addition.

2.2. Characterization

Powder X-ray diffraction (XRD) was measured by an X-ray diffractometer (X'pert pro MPD, Almelo, The Netherlands) with Cu K α (40 kV, 40 mA) radiation. High-resolution transmission electron microscopy (HR-TEM) images and selected-area electron diffraction (SAED) patterns were obtained using field emission (JEOL JEM-2100, Tokyo, Japan) at the KBSi Busan Center. Fourier transform infrared spectroscopy (FTIR) spectra were recorded using a Vertex 80 v FTIR spectrometer (Bruker, Billerica, MA, USA) over the range of 400–4000 cm⁻¹ with KBr pellets.

X-ray absorption spectroscopy experiments were conducted at the Ce L₃-edge using the extended X-ray absorption fine structure (EXAFS) facility of the 10C-wide XAFS beam line at the Pohang Accelerator Laboratory (Pohang, Korea). The storage ring was operated at 2.5 GeV with an injection current of 251 mA using a Si (111) double-crystal monochromator. The X-ray absorption spectroscopy (XAFS) data at the Ce L₃ edge were collected at room temperature in transmission mode. The background intensity was removed and normalized using Fourier transform under k-weight 3 to measure the interatomic distance. The XAFS data were analyzed using the Athena and Artemis software packages.

The Brunauer–Emmett–Teller (BET) surface area was measured by N₂ adsorption/desorption with a Micromeritics 2020 M instrument (Micromeritics, Norcross, GA, USA). H₂ temperature-programmed reduction (H₂-TPR) was performed using a Quantachrome with a Chem BET chemisorption analyzer (Micromeritics, Norcross, GA, USA) with 100 mg of the sample in a quartz tube reactor with a thermal conductivity detector (TCD). The sample was preheated from room temperature to 200 °C for 1 h and then cooled down to room temperature. TPR was performed at 10 °C/min up to 800 °C using 10 vol% H₂ in He gas. CuO was used as a reference for calibration to quantify the total amount of H₂ consumed.

3. Results and Discussion

The crystallinity and phase of the synthesized CeO₂-TiO₂ were investigated by XRD analysis, as shown in Figure 1, and each pattern corresponded to CT and CT_H₂O₂. Anatase

TiO₂ and CeO₂ peaks were confirmed in the CT pattern, revealing that CT consisted of CeO₂ and TiO₂ and that there were no secondary peaks. On the other hand, the broadening of those peaks was observed in the pattern of CT_H₂O₂ compared to CT, indicating that CT_H₂O₂ had a low crystallinity of CeO₂ and TiO₂ or consisted of very small nanoparticles. This finding is similar to that of previous studies, indicating that CT_H₂O₂ had very low crystallinity through a broad peak and a low intensity [18,19]. Further analysis was performed to examine the structure of the CeO₂-TiO₂ changed by H₂O₂.

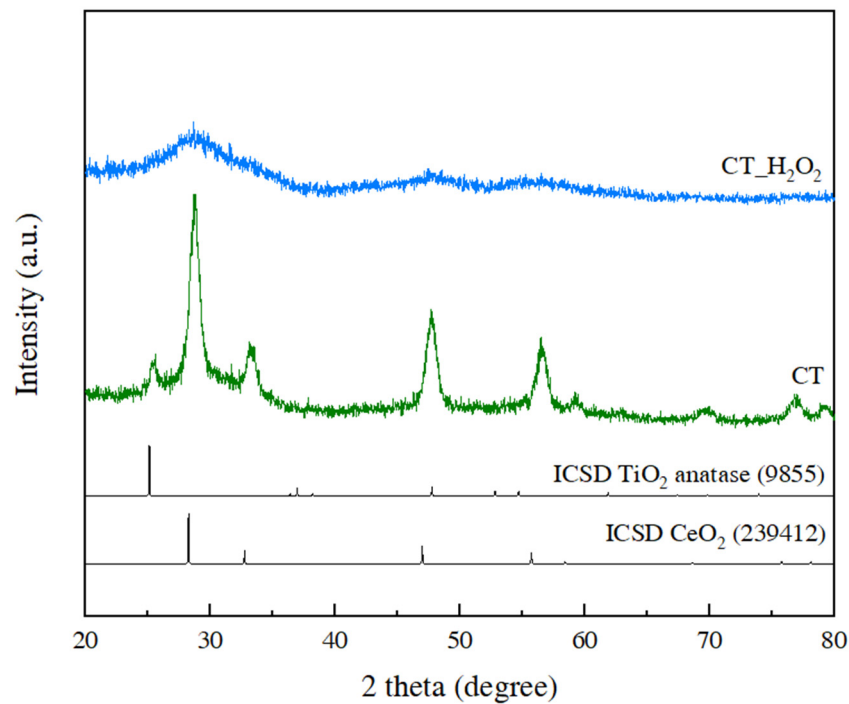


Figure 1. XRD patterns of CT and CT_H₂O₂.

The microstructure and crystallinity of CT and CT_H₂O₂ were verified through TEM images and SAED patterns, as displayed in Figure 2. Particles of approximately 10 nm with lattice fringes were observed in the TEM image of CT, indicating that they had a crystalline structure (Figure 2a). These crystalline structures were composed of a CeO₂ (111) plane with an interplanar spacing of 0.31 nm and a TiO₂ (101) plane with a 0.35 nm interplanar spacing. The SAED pattern of CT showed ring patterns, meaning that CT existed in crystalline form (Figure 2b). In contrast, an amorphous structure was found in the TEM image of CT_H₂O₂ (Figure 2c), and a diffuse ring pattern was confirmed (Figure 2d). Based on these results, H₂O₂ addition was the cause of the amorphization of CeO₂-TiO₂.

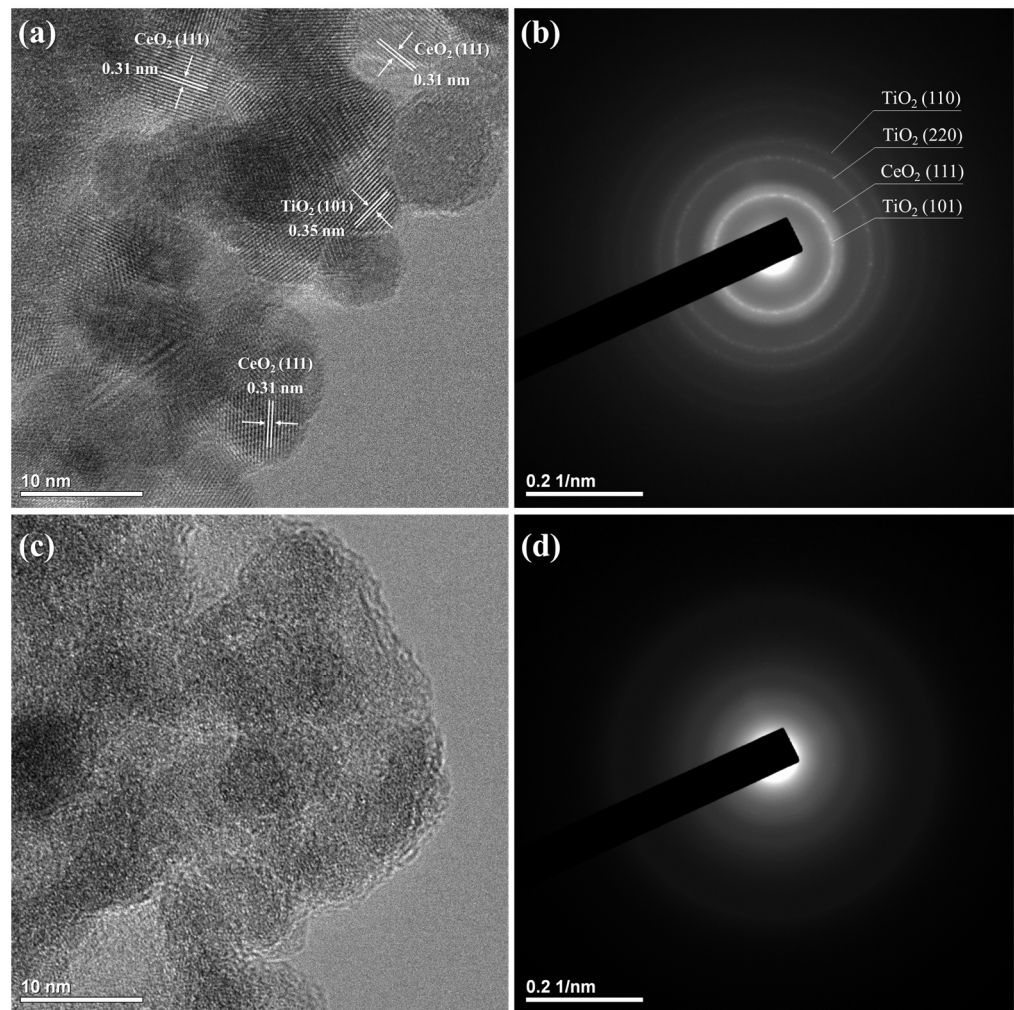


Figure 2. TEM images and SAED patterns of (a,b) CT and (c,d) CT_{H₂O₂}.

FTIR analysis was carried out to investigate the effect of H₂O₂ on CeO₂-TiO₂ linkage formation in sol-gel chemistry. The calcination process is generally necessary in the sol-gel synthesis of oxides, and impurities—including OH groups and organic matter—are removed when calcination is performed for precipitation [20]. The FTIR spectra of CT and CT_{H₂O₂} before and after calcination are shown in Figure 3, and all peaks were classified through the literature [21–25]. The characteristic absorption peak of TTIP was in the range of 1085–1050 cm⁻¹. Since characteristic peaks were not detected for all samples, all TTIPs participated in the sol-gel reaction. A reduced CH₃ peak at 1338 cm⁻¹ revealed that the organic matter was removed by calcination. Peaks assigned to the -OH group appeared at 3542 cm⁻¹ and 1630 cm⁻¹, and the peak intensities of the samples before calcination were greater than those after calcination. It should be noted that CT_{H₂O₂} had stronger OH peaks than CT and had an O–O peak representing a peroxy group at 900 cm⁻¹. In addition, the Ce–O₂²⁻ peak at 842 cm⁻¹ demonstrated that H₂O₂ formed O₂²⁻ [26]. The difference between the OH peaks of CT and CT_{H₂O₂} is explained by O₂²⁻ (peroxy ions).

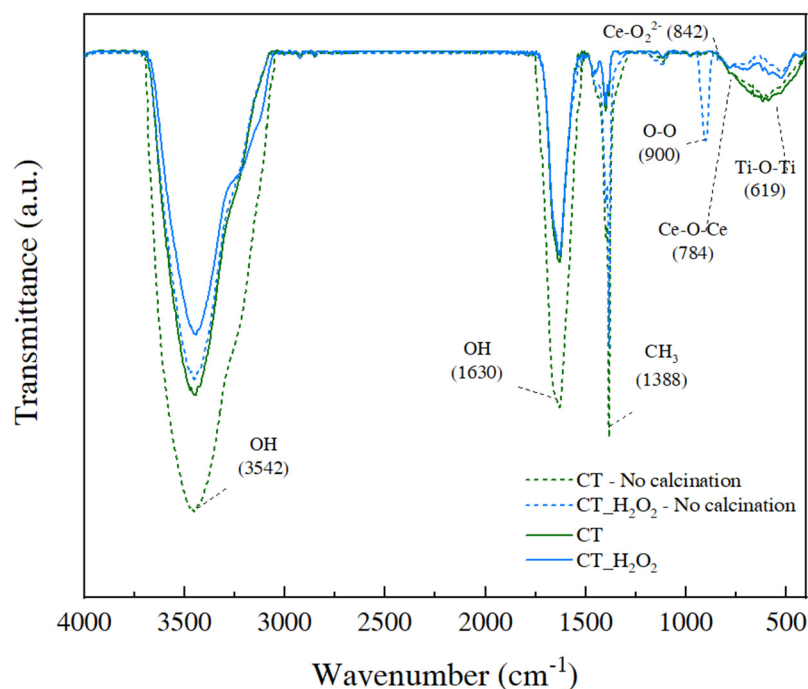


Figure 3. FTIR spectra of CT and CT_H₂O₂ before calcination.

The Ce-O-Ce and Ti-O-Ti peaks in the fingerprint region of 800 to 400 cm⁻¹ indicate the metal–oxygen linkage and bonding network. The one large peak in this region is due to the Ce-O-Ti linkage, confirming that the cerium species react via a cross-link and covalently bond on the Ti-O-Ti [25,27]. A wide peak in this region in the CT spectrum indicated a large network [28]. The intensity of this peak decreased after adding H₂O₂, and the intensity of this peak indicates the size of the Ce-O-Ce or Ti-O-Ti network. This decrease occurred because O₂²⁻ interfered with the hydrolysis and condensation reactions and thus affected the formation of the Ti-O-Ti network.

EXAFS is a powerful technique for analyzing the local structure of amorphous materials [26]. The EXAFS $k_3\chi$ data and Fourier transform (F.T.) of Ce L₃ edge are shown in Figure 4. It was confirmed that CT had a long-range order but that CT_H₂O₂ had a short-range order resulting from the broken order. As corresponding results, the oscillation differences between CT and CT_H₂O₂ were clearly seen in the red dotted circle of the k space at the Ce L₃-edge (Figure 4a), and severe noise due to the disordered structure of the amorphous phase was observed. EXAFS F.T. data at the Ce L₃ edge (Figure 4b) provide information on the bond length and the disordering around the Ce atoms. The first and third peaks are assigned to the 1st shell and 2nd shell, respectively, indicating the distances between the Ce-O and Ce-Ce atoms. The second peak is the Ce-Ti bond assigned to an interaction between Ce-Ti forming amorphous Ce [29]. In CT, the bonding length of Ce-O was 1.84 Å and that of Ce-Ce was 3.53 Å. For CT_H₂O₂, the bond length of Ce-O decreased to 1.68 Å, and no Ce-Ce peak was observed. Additionally, the broadening of the 1st shell peak was confirmed with the addition of H₂O₂, which is related to amorphization due to disordering, revealing the disordering of the oxygen around Ce [30]. The peak intensity ratio of the 1st shell and the 2nd shell (I_{2nd}/I_{1st}) indicates the degree of amorphousness, and this ratio decreased from 0.56 to 0.15, indicating amorphization by H₂O₂.

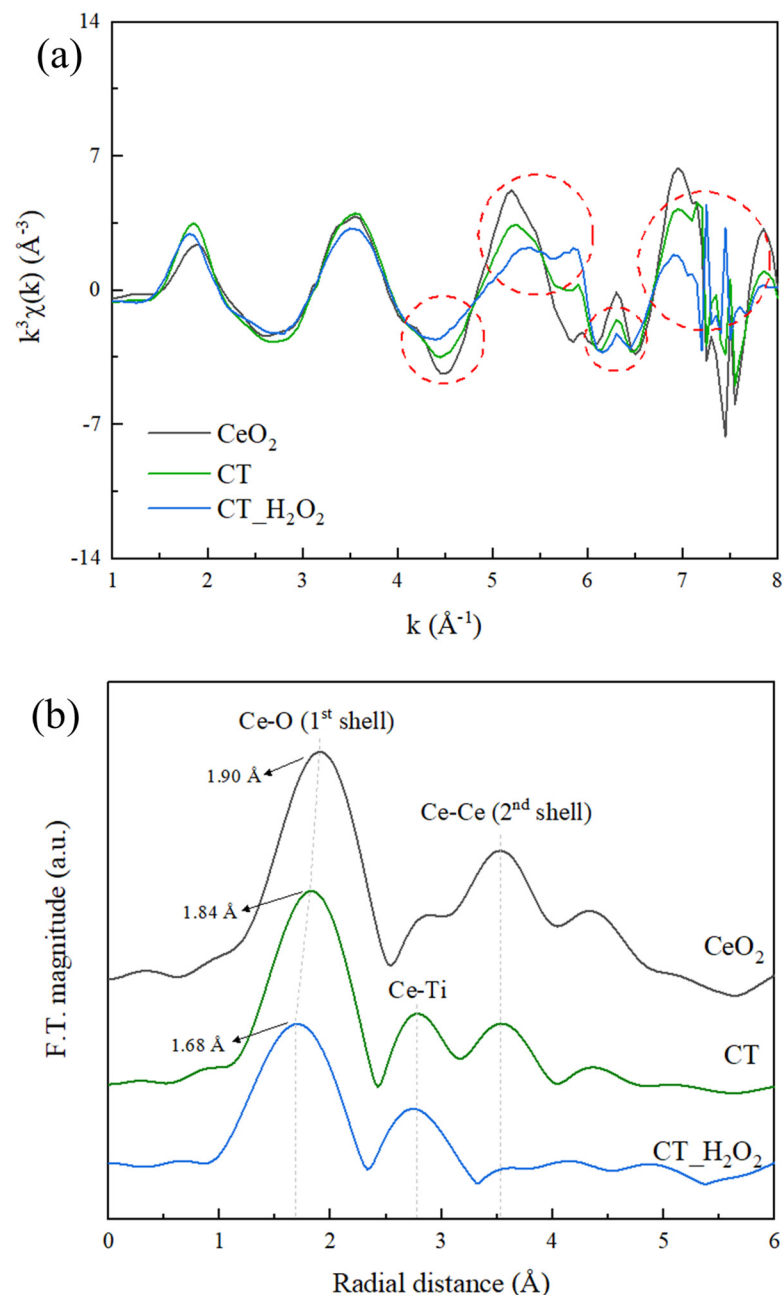
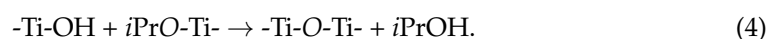
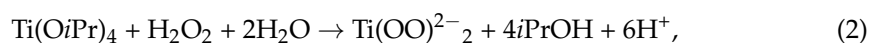
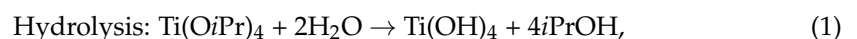


Figure 4. (a) Extended X-ray absorption fine structure (EXAFS) $k_3\chi$ data and (b) Fourier transform of the EXAFS $k_3\chi$ data at the Ce L_3 -edge EXAFS of CT and $\text{CT}_{\text{H}_2\text{O}_2}$.

This disordering occurs because the strong nucleophilicity of O_2^{2-} causes strong bonding with Ti ions, which interferes with the binding of OH (Figure 5). In more detail, this could be described as the hydrolysis reaction (Equations (1) and (2)) and condensation reaction (Equations (3) and (4)) in sol-gel chemistry [15,17].



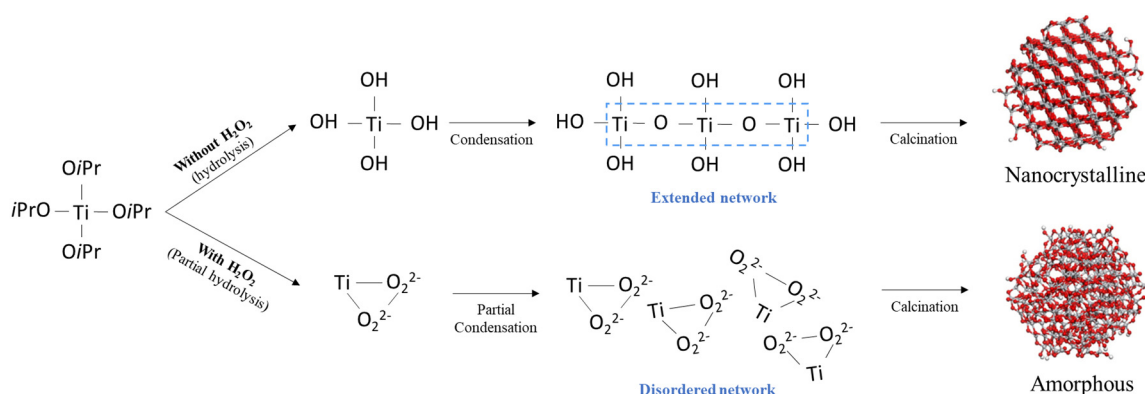


Figure 5. Schematic showing the effect of H_2O_2 on the local structure.

TTIP ($\text{Ti}(\text{OiPr})_4$) reacts with H_2O and a hydrolysis reaction occurs to form $-\text{Ti}-\text{OH}$ (Equation (1)). The condensation reaction also simultaneously occurs to release one H_2O or $i\text{PrOH}$ molecule, forming an extended network of $\text{Ti}-\text{O}-\text{Ti}$ (Equations (3) and (4)). In the H_2O_2 addition, O_2^{2-} is strongly bound to Ti ions, eventually inhibiting the binding to OH (Equation (2)). As a result, the hydrolysis and condensation reactions of TTIP would have partially occurred. It is concluded that the extended network of $\text{Ti}-\text{O}-\text{Ti}$ was not formed due to partial hydrolysis by O_2^{2-} , leading to amorphization.

The redox properties of $\text{CeO}_2\text{-TiO}_2$ according to amorphization were analyzed by H_2 -TPR, and the results are illustrated in Figure 6. The H_2 consumption and specific surface area were 1110 mmol/g and 103.0 m^2/g for CT, and 1354 mmol/g and 113.1 m^2/g for CT- H_2O_2 , respectively as shown in Table 1. This is due to the smaller particle size of CT- H_2O_2 or the formation of dangling bonds due to the disordering of $\text{Ce}-\text{O}$ [31–33]. These two facts suggest that the active surface area of CT- H_2O_2 is larger. CT had two peaks observed at 490 $^\circ\text{C}$ and 767 $^\circ\text{C}$, which corresponded to the reduction from Ce^{4+} to Ce^{3+} by the surface oxygen of CeO_2 and the lattice oxygen of CeO_2 , respectively [34]. CT- H_2O_2 showed a peak due to the surface oxygen at only 468 $^\circ\text{C}$ and 558 $^\circ\text{C}$, and there was no reduction peak assigned to the lattice CeO_2 , which implies that CT- H_2O_2 is amorphous [35,36]. The surface CeO_2 peak shifted to low temperature by amorphization, and the H_2 consumption increased, confirming the improvement of the redox property. The atoms of the crystalline oxide are tightly bonded by strong intermolecular forces, while the atoms of the amorphous oxide are loosely bonded. Consequently, the improvement of the redox property was because the $\text{Ce}-\text{O}-\text{Ce}$ bond was weak and easily reduced by the disordered structure of CT- H_2O_2 .

Table 1. H_2 -TPR results and BET surface area of CT and CT- H_2O_2 .

Sample	Surface Oxygen Reduction Temp. ($^\circ\text{C}$)	Bulk Oxygen Reduction Temp. ($^\circ\text{C}$)	H_2 Consumption (mmol/g)	BET Surface Area (m^2/g)
CT	490	797	1110	103.0
CT- H_2O_2	468	Not observed	1354	113.1

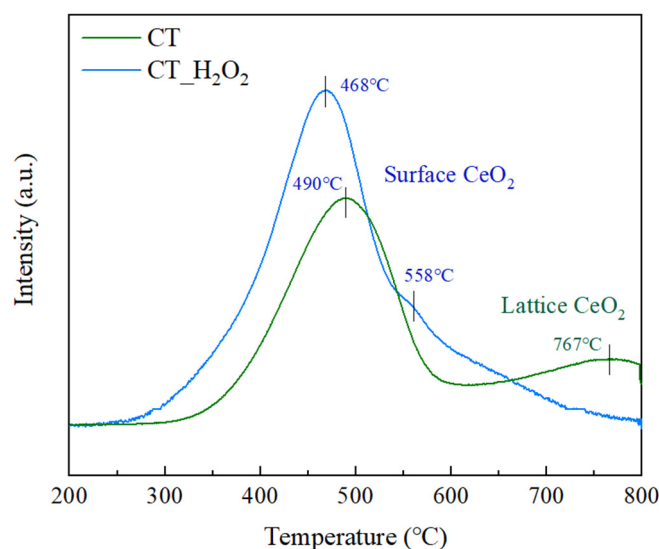


Figure 6. H₂-TPR profiles of CT and CT_H₂O₂.

4. Conclusions

We studied the effect of H₂O₂ on the Ce-O-Ti linkage in the sol-gel reaction in terms of local structure for the first time. The decrease in the crystallinity of CeO₂-TiO₂ with the addition of H₂O₂ was verified through XRD peak broadening, and it was confirmed that the SAED pattern of CeO₂-TiO₂ became a diffuse pattern. CeO₂ and crystalline TiO₂ were observed for CT, whereas an amorphous structure was observed for CT_H₂O₂. In the FTIR spectrum of CT_H₂O₂, the O₂²⁻ peak attributed to H₂O₂ was observed, and the broadening of the metal-oxygen peak showed that the size of the metal-oxygen network decreased due to O₂²⁻. The local structure of the synthesized samples was analyzed using EXAFS. Severe noise and oscillation differences in the k space were observed by the disordered structure in CT_H₂O₂; furthermore, the decrease in the Ce-O bond length and the broadening of the Ce-O peak in R space were identified. It was found that O₂²⁻ interfered with the formation of the metal-oxygen extended network. In the H₂-TPR analysis to investigate the redox property according to the amorphization, a low-temperature shift in the surface CeO₂ reduction peak and an increase in H₂ consumption indicated an improvement in the redox property due to amorphization. The improved redox property of amorphous CeO₂-TiO₂ resulted from the metal-oxygen bond being weakened by disordered oxygen.

Author Contributions: Conceptualization, H.L.; Formal analysis, M.K.; Investigation, M.K., G.P. and H.L.; Methodology, M.K. and G.P.; Supervision, H.L.; Visualization, M.K.; Writing—original draft, M.K.; Writing—review & editing, G.P. and H.L. All authors have read and agreed to the published version of the manuscript.

Funding: This research was supported by the Korea Ministry of Trade, Industry, and Energy (MOTIE) as “Development of NO_x Removal Catalyst with Wide Temperature Window (No.20005721)”. This research was supported by the BK21 FOUR Program (NO.4120200513801) funded by the Ministry of Education(MOE, Korea) and National Research Foundation of Korea(NRF).

Data Availability Statement: The data presented in this study are available on request from the corresponding author.

Conflicts of Interest: The authors declare no conflict of interest.

References

- Oskam, G. Metal oxide nanoparticles: Synthesis, characterization and application. *J. Sol-Gel Sci. Technol.* **2006**, *37*, 161–164. [[CrossRef](#)]
- Trovarelli, A.; Boaro, M.; Rocchini, E.; de Leitenburg, C.; Dolcetti, G. Some recent developments in the characterization of ceria-based catalysts. *J. Alloys Compd.* **2001**, *323*, 584–591. [[CrossRef](#)]

3. Li, P.; Xin, Y.; Li, Q.; Wang, Z.; Zhang, Z.; Zheng, L. Ce–Ti amorphous oxides for selective catalytic reduction of NO with NH₃: Confirmation of Ce–O–Ti active sites. *Environ. Sci. Technol.* **2012**, *46*, 9600–9605. [[CrossRef](#)]
4. Fang, N.; Ding, Y.; Liu, C.; Chen, Z. Effect of crystalline/amorphous structure on light absorption and carrier separation of CeO₂-TiO₂ heterojunctions. *Appl. Surf. Sci.* **2018**, *452*, 49–57. [[CrossRef](#)]
5. Zhu, H.; Qin, Z.; Shan, W.; Shen, W.; Wang, J. Pd/CeO₂-TiO₂ catalyst for CO oxidation at low temperature: A TPR study with H₂ and CO as reducing agents. *J. Catal.* **2004**, *225*, 267–277. [[CrossRef](#)]
6. Curry-Hyde, H.E.; Musch, H.; Baiker, A. Selective catalytic reduction of nitric oxide over amorphous and crystalline chromia: I. Comparative study of activities. *Appl. Catal.* **1990**, *65*, 211–223. [[CrossRef](#)]
7. Tang, X.; Hao, J.; Xu, W.; Li, J. Low temperature selective catalytic reduction of NO_x with NH₃ over amorphous MnO_x catalysts prepared by three methods. *Catal. Commun.* **2007**, *8*, 329–334. [[CrossRef](#)]
8. Li, L.; Shao, Q.; Huang, X. Amorphous oxide nanostructures for advanced electrocatalysis. *Chem. Eur. J.* **2020**, *26*, 3943–3960. [[CrossRef](#)]
9. Gao, X.; Jiang, Y.; Zhong, Y.; Luo, Z.; Cen, K. The activity and characterization of CeO₂-TiO₂ catalysts prepared by the sol-gel method for selective catalytic reduction of NO with NH₃. *J. Hazard. Mater.* **2010**, *174*, 734–739. [[CrossRef](#)]
10. Tian, J.; Sang, Y.; Zhao, Z.; Zhou, W.; Wang, D.; Kang, X.; Liu, H.; Wang, J.; Chen, S.; Cai, H.; et al. Enhanced photocatalytic performances of CeO₂/TiO₂ nanobelt heterostructures. *Small* **2013**, *9*, 3864–3872. [[CrossRef](#)]
11. Gao, X.; Jiang, Y.; Fu, Y.; Zhong, Y.; Luo, Z.; Cen, K. Preparation and characterization of CeO₂/TiO₂ catalysts for selective catalytic reduction of NO with NH₃. *Catal. Commun.* **2010**, *11*, 465–469. [[CrossRef](#)]
12. Frenzer, G.; Maier, W.F. Amorphous porous mixed oxides: Sol-gel ways to a highly versatile class of materials and catalysts. *Annu. Rev. Mater. Res.* **2006**, *36*, 281–331. [[CrossRef](#)]
13. Simonsen, M.E.; Søgaard, E.G. Sol-gel reactions of titanium alkoxides and water: Influence of pH and alkoxy group on cluster formation and properties of the resulting products. *J. Sol-Gel Sci. Technol.* **2010**, *53*, 485–497. [[CrossRef](#)]
14. Debecker, D.P.; Mutin, P.H. Non-hydrolytic sol-gel routes to heterogeneous catalysts. *Chem. Soc. Rev.* **2012**, *41*, 3624–3650. [[CrossRef](#)] [[PubMed](#)]
15. Seok, S.I.; Ahn, B.Y.; Pramanik, N.C.; Kim, H.; Hong, S.I. Preparation of nanosized rutile TiO₂ from an aqueous peroxotitanate solution. *J. Am. Ceram. Soc.* **2006**, *89*, 1147–1149. [[CrossRef](#)]
16. Shen, C.; Shaw, L.L. FTIR analysis of the hydrolysis rate in the sol-gel formation of gadolinia-doped ceria with acetylacetonate precursors. *J. Sol-Gel Sci. Technol.* **2010**, *53*, 571–577. [[CrossRef](#)]
17. Livage, J.; Sanchez, C. Sol-gel chemistry. *J. Non-Cryst. Solids* **1992**, *145*, 11–19. [[CrossRef](#)]
18. Li, S.; Xu, Q.; Uchaker, E.; Cao, X.; Cao, G. Comparison of amorphous, pseudo-hexagonal and orthorhombic Nb₂O₅ for high-rate lithium ion insertion. *CrystEngComm* **2016**, *18*, 2532–2540. [[CrossRef](#)]
19. Zou, J.; Gao, J.; Xie, F. An amorphous TiO₂ sol sensitized with H₂O₂ with the enhancement of photocatalytic activity. *J. Alloys Compd.* **2010**, *497*, 420–427. [[CrossRef](#)]
20. Gao, Y.; Masuda, Y.; Seo, W.S.; Ohta, H.; Koumoto, K. TiO₂ nanoparticles prepared using an aqueous peroxotitanate solution. *Ceram. Int.* **2004**, *30*, 1365–1368. [[CrossRef](#)]
21. Mohammadi, M.R.; Fray, D.J. Nanostructured TiO₂-CeO₂ mixed oxides by an aqueous sol-gel process: Effect of Ce: Ti molar ratio on physical and sensing properties. *Sens. Actuators B Chem.* **2010**, *150*, 631–640. [[CrossRef](#)]
22. Sharma, N.; Deepa, M.; Varshney, P.; Agnihotry, S.A. FTIR and absorption edge studies on tungsten oxide based precursor materials synthesized by sol-gel technique. *J. Non-Cryst. Solids* **2002**, *306*, 129–137. [[CrossRef](#)]
23. Damatov, D.; Mayer, J.M. (Hydro)peroxide ligands on colloidal cerium oxide nanoparticles. *Chem. Commun.* **2016**, *52*, 10281–10284. [[CrossRef](#)]
24. Alsharaeh, E.H.; Bora, T.; Soliman, A.; Ahmed, F.; Bharath, G.; Ghoniem, M.G.; Abu-Salah, K.M.; Dutta, J. Sol-gel-assisted microwave-derived synthesis of anatase Ag/TiO₂/GO nanohybrids toward efficient visible light phenol degradation. *Catalysts* **2017**, *7*, 133. [[CrossRef](#)]
25. Wandre, T.M.; Gaikwad, P.N.; Tapase, A.S.; Garadkar, K.; Vanalakar, S.A.; Lokhande, P.D.; Sasikala, R.; Hankare, P.P. Sol-gel synthesized TiO₂-CeO₂ nanocomposite: An efficient photocatalyst for degradation of methyl orange under sunlight. *J. Mater. Sci. Mater. Electron.* **2016**, *27*, 825–833. [[CrossRef](#)]
26. Sanchez, C.; Livage, J.; Henry, M.; Babonneau, F. Chemical modification of alkoxide precursors. *J. Non-Cryst. Solids* **1988**, *100*, 65–76. [[CrossRef](#)]
27. Purcar, V.; Rădițoiu, V.; Nicolae, C.A.; Frone, A.N.; RĂDIȚOIU, A.; Raduly, F.M.; ȘOMOGHI, R.; Gabor, R.A.; Căprărescu, S. Synthesis and morpho-structural properties of TiO₂-based materials. *J. Optoelectron. Adv. Mater.* **2019**, *21*, 281–286.
28. Ksapabutr, B.; Gulari, E.; Wongkasemjit, S. Sol-gel derived porous ceria powders using cerium glycolate complex as precursor. *Mater. Chem. Phys.* **2006**, *99*, 318–324. [[CrossRef](#)]
29. Teo, B.K. *EXAFS: Basic Principles and Data Analysis*; Springer Science & Business Media: Berlin/Heidelberg, Germany, 2012; Volume 9.
30. Jo, S.H.; Lee, H. Local structure and short-range ordering of MnO₂-Ce_(1-x)Zr_xO₂/TiO₂. *Mater. Charact.* **2015**, *110*, 102–108. [[CrossRef](#)]
31. Jo, S.H.; Lee, I.; Park, H.; Lee, H. Experimental evidence and mechanism of the oxygen storage capacity in MnO₂-Ce_(1-x)Zr_xO₂/TiO₂ catalyst for low-temperature SCR. *Ceram. Int.* **2017**, *43*, 5182–5188. [[CrossRef](#)]

32. Vayssilov, G.N.; Lykhach, Y.; Migani, A.; Staudt, T.; Petrova, G.P.; Tsud, N.; Skála, T.; Bruix, A.; Illas, F.; Prince, K.C.; et al. Support nanostructure boosts oxygen transfer to catalytically active platinum nanoparticles. *Nat. Mater.* **2011**, *10*, 310–315. [[CrossRef](#)] [[PubMed](#)]
33. Park, G.; Kim, M.; Cha, J.; Kim, H.; Lee, H. Local atomic structure and enhanced catalytic activity of W doped CeWTiOx catalysts. *J. Solid State Chem.* **2020**, *292*, 121689. [[CrossRef](#)]
34. Neri, G.; Pistone, A.; Milone, C.; Galvagno, S. Wet air oxidation of p-coumaric acid over promoted ceria catalysts. *Appl. Catal. B Environ.* **2002**, *38*, 321–329. [[CrossRef](#)]
35. Liu, J.; Wang, L.L.; Fei, Z.Y.; Chen, X.; Tang, J.H.; Cui, M.F.; Qiao, X. Structure and properties of amorphous CeO₂@TiO₂ catalyst and its performance in the selective catalytic reduction of NO with NH₃. *J. Fuel Chem. Technol.* **2016**, *44*, 954–960. [[CrossRef](#)]
36. Fei, Z.; Yang, Y.; Wang, M.; Tao, Z.; Liu, Q.; Chen, X.; Cui, M.; Zhang, Z.; Tang, J.; Qiao, X. Precisely fabricating Ce-O-Ti structure to enhance performance of Ce-Ti based catalysts for selective catalytic reduction of NO with NH₃. *Chem. Eng. J.* **2018**, *353*, 930–939. [[CrossRef](#)]